RSC Advances

PAPER

View Article Online
View Journal | View Issue



Cite this: *RSC Adv.*, 2023, **13**, 14841

# Modulated wafer-scale $WS_2$ films based on atomic-layer-deposition for various device applications†

Xiangyu Guo,[a] Hanjie Yang,[a] Xichao Mo,[b] Rongxu Bai,[a] Yanrong Wang,[b] Qi Han,[a] Sheng Han,[a] Qingqing Sun,[a] David W. Zhang,[a] Shen Hu *[ac] and Li Ji*[ad]

Received 11th February 2023
Accepted 9th May 2023

DOI: 10.1039/d3ra00933e

rsc.li/rsc-advances

Tungsten disulfide ($WS_2$) is promising for potential applications in transistors and gas sensors due to its high mobility and high adsorption of gas molecules onto edge sites. This work comprehensively studied the deposition temperature, growth mechanism, annealing conditions, and Nb doping of $WS_2$ to prepare high-quality wafer-scale N- and P-type $WS_2$ films by atomic layer deposition (ALD). It shows that the deposition and annealing temperature greatly influence the electronic properties and crystallinity of $WS_2$, and insufficient annealing will seriously reduce the switch ratio and on-state current of the field effect transistors (FETs). Besides, the morphologies and carrier types of $WS_2$ films can be controlled by adjusting the processes of ALD. The obtained $WS_2$ films and the films with vertical structures were used to fabricate FETs and gas sensors, respectively. Among them, the $I_{on}/I_{off}$ ratio of N- and P-type $WS_2$ FETs is $10^5$ and $10^2$, respectively, and the response of N- and P-type gas sensors is 14% and 42% under 50 ppm $NH_3$ at room temperature, respectively. We have successfully demonstrated a controllable ALD process to modify the morphology and doping behavior of $WS_2$ films with various device functionalities based on acquisitive characteristics.

## 1. Introduction

Transition metal dichalcogenides (TMDs) have attracted much attention due to their appropriate band gaps, good stability in ambient conditions, and excellent electronic/optoelectronic characteristics.[1–5] They have been highlighted as promising materials that can exceed the current limitation of traditional materials.[6,7] TMDs are compounds composed of transition metal elements and chalcogenide elements, whose chemical structural formula can be expressed as $MX_2$, M represents transition metal elements, and X represents chalcogenide elements.[8] Among the family of TMDs, $WS_2$ has superior properties thanks to its relatively high carrier mobility, large exciton binding energy, large spin–orbit splitting, and strong photoluminescence.[9–13] The theoretical mobility of monolayer $WS_2$ at room temperature is ~250 $cm^2\ V^{-1}\ s^{-1}$.[14,15] With the increase of layer numbers, $WS_2$ will change from direct bandgap (1.8–2.1 eV) for monolayer to indirect bandgap (1.3–1.4 eV) for bulk.[16,17] In addition, $WS_2$ has a high specific surface area, availability of active gas adsorption sites (edge, sulfur defects, and vacancy), and high absorption coefficient.[18] These properties make it ideal for many applications, such as transistors,[19,20] gas sensors,[21,22] photodetectors,[23] and light-emitting devices.[24]

In order to fully realize its practical device-level applications on a large scale, it is necessary to deposit wafer-scale ultra-thin films with high uniformity below 10 nm.[25] ALD is ideal for sub-10 nm film growth with unique and superior growth characteristics, such as wafer-scale growth, excellent uniformity, and CMOS process compatibility.[26,27] In addition, compared with CVD, a common technique for TMDs studies in lab scale, ALD holds many advantages, such as precise controllability (*e.g.*, thickness, morphology, and doping),[28,29] low deposition temperature, and excellent step coverage,[30] all of which that are beneficial for the construction of advanced non-planar geometry devices like Fin-FETs and gate-all-around FETs.[31] ALD is based on a self-limiting growth mechanism, and a thin film is formed on a substrate surface by surface adsorption and chemical reaction.[32] However, TMD's unconventional surface chemistry makes it sensitive to external conditions during growth. The lack of hanging bonds on the surface of TMDs leads to the absence of adsorption and reaction sites required for ALD growth, thus TMD thin film deposition on with excellent uniformity is quite a challenge.[33]

In our previous work, the morphology and Nb-doped level of $WS_2$ thin films can be regulated by ALD.[28,29] It has been found that the vertical structure of $WS_2$ can reduce the performance of FETs. However, complex morphology is very important for gas sensors. Building on previous studies, FETs and gas sensors are

[a]*School of Microelectronics, Fudan University, Shanghai 200433, China. E-mail: hushen@fudan.edu.cn; lji@fudan.edu.cn*

[b]*School of Physical Science and Technology, Lanzhou University, Lanzhou 730000, China*

[c]*Jiashan Fudan Institute, Jiashan 314100, China*

[d]*Hubei Yangtz Memory Laboratories, Wuhan 430205, China*

† Electronic supplementary information (ESI) available. See DOI: https://doi.org/10.1039/d3ra00933e

prepared according to the characteristics of $WS_2$ films, respectively. And the effects of the growth temperature on the morphology and elemental properties for $WS_2$ films were studied, followed by post-annealing to obtain high-quality $WS_2$ films. The morphology of the samples in different deposition cycles was characterized by atomic force microscope (AFM) and scanning electron microscopy (SEM), and the growth process of island, horizontal and vertical was analyzed. In the horizontal growth stage, the $WS_2$ film is an ideal channel material for transistors and is used to fabricate top-gated transistor arrays with $I_{on}/I_{off}$ ratio of $10^5$ and the mobility of 7.25 $cm^2 V^{-1} s^{-1}$. In the vertical growth stage, $WS_2$ has abundant edge exposure sites and ideal active sites due to its vertical structure, which has been used to prepare $NH_3$ sensors. In addition, the introduction of *in situ* $NbS_2$ deposition cycles can effectively change the carrier type. The mobility of P-type FET is 0.23 $cm^2 V^{-1} s^{-1}$, the $I_{on}/I_{off}$ ratio is $10^2$, and the responsiveness of the gas sensor based on P-type films is 42%@50 ppm $NH_3$ under room temperature. This study proves that $WS_2$ films prepared by ALD have outstanding controllability in morphology and doping, which can be well applied to FETs and gas sensors. The functional application of $WS_2$ will benefit the development and commercialization for next-generation electronic devices.

# 2. Experimental

## 2.1 Sample preparation

**2.1.1 Deposition of $WS_2$ film.** The $WS_2$ and Nb-doped $WS_2$ films were deposited on a 2-inch sapphire substrate by ALD (Beneq, TFS-200). Before the deposition, the sapphire substrate was cleaned with acetone, ethyl alcohol, diluted HF (1 : 50), and deionized water.

For $WS_2$ films, Ar (99.99%) gas was purged into a reactor between the $WCl_6$ (99.9%) and $(CH_3)_3SiSSi(CH_3)_3$ (HMDST, 98%) pulse steps. The $WCl_6$ temperature was kept at 93 °C, while the HMDST was kept at room temperature. One cycle of ALD $WS_2$ deposition included 1 s $WCl_6$ pulse time, followed by 10 s of purge time (Ar, 99.99%) and 1 s of HMDST pulse time, followed by 5 s of purge time, respectively.

For Nb doping, a typical $NbS_2$ process cycle included 1 s $NbCl_5$ pulse, followed by 8 s purge (Ar, 99.99%), and 1 s HMDST pulse, followed by 5 s purge. To achieve Nb-doped $WS_2$ film, the $NbS_2$ process was sandwiched into a $WS_2$ process accordingly.

**2.1.2 Annealed of $WS_2$ film.** The as-deposited samples were placed in a quartz boat at the center of Zone II, and 0.5 g sulfur powder was placed in Zone III carried by a quartz boat (as shown in Fig. S1†). Argon (10 sccm, 99.999%) was chosen as the carrier gas. The samples were annealed for 2 h in a 4-inch quartz tube at a base pressure of 10 Pa.

**2.1.3 FETs fabrication.** Annealed $WS_2$ films were first patterned by ultraviolet lithography to define the active area, with LOR 3A and S1813 as the adhesive and photoresist, respectively. $CF_4$ and Ar plasma were then used for etching in reactive ion etching (RIE, 40/10 sccm, 150 W, 2 min). After removing the photoresistor with acetone, the source and drain were patterned by lithography and physical vapor deposition (10/70 nm Ti/Au for N- type FETs and 10/70 nm Ti/Pt for P-type FETs), followed by a lift-off process. With trimethylaluminum and $H_2O$ as precursors, a 30 nm $Al_2O_3$ gate dielectric layer was grown at 250 °C using a Beneq TFS-200 ALD system. Finally, the 10/70 nm Ti/Au top-gate electrodes were formed using the same process as the source/drain electrodes. Devices with a channel size of 50/10 μm (W/L) (detailed doping process in Fig. S2†).

**2.1.4 Gas sensors fabrication.** The Ti/Au electrodes with 10 nm/70 nm thickness were deposited on the $WS_2$ films using electron beam evaporation. A stainless steel shadow mask was used to form the patterns of electrodes on the $WS_2$ film. The electrodes had a channel width/length ratio of 100 and channel length of 100 μm.

## 2.2 Characterization methods

**2.2.1 Materials characterization.** The morphology and structure of $WS_2$ and Nb-doped $WS_2$ were characterized by SEM (ZEISS GeminiSEM 300, signal is collected by Inlens secondary electron detector) and AFM (Horiba Labram HR evolution Aist-NT); XPS (Augerscan PHI5300, monochromatic Al Kα anode at 9.97 kV and 14.7 mA as the source of X-ray radiation; pass energy was 112 eV; the step was 0.1 eV, peak fitted using combined Gaussian, and Lorentzian line shapes), Raman (LabRAM, 532 nm laser wavelength, 1 mW × 100_VIS), and HRTEM (Thermo Fisher Scientific Talos F200X; acceleration voltage was 200 kV; the sample was prepared by Thermo Fisher Scientific Helios G4 UX focus ion beam, and a protective layer of Pt was deposited on the surface of the sample by electron beam and ion beam).

**2.2.2 Device measurement.** The electrical properties of FETs were measured at ambient room temperature by the Agilent B1500A Semiconductor Device Analyzer in the probe station (MPITS3000). The mobility of FETs can be extracted from the transfer curve using the following equation: $\mu = (\Delta I_{DS}/\Delta V_{GS}) \times L/(W_{C_{ox}} V_{DS})$, where $L$ and $W$ are the channel length and width, $C_{ox} = \varepsilon_1\varepsilon_0/d$ was the capacitance between the drain and the gate per unit area, $\varepsilon_1$, $\varepsilon_0$ are the dielectric constants of the $Al_2O_3$ layer and vacuum, and $d$ is the thickness of the high-$k$ dielectric.

# 3. Results and discussion

## 3.1 Deposition of wafer-scale $WS_2$

Fig. 1a shows one typical cycle of the ALD synthesis process for $WS_2$. $WCl_6$ and HMDST precursors are introduced into the reaction chamber by Ar as carrier gas. $WS_2$ films grown on sapphire substrates in a self-limiting reaction. In Fig. 1b, $WS_2$ films were etched by RIE to characterize film thickness. AFM result shows that the thickness of 400 cycles $WS_2$ film is 5.50 nm at 400 °C deposition temperature. Fig. 1c illustrates the thicknesses at nine locations across the 2-inch wafer, with a minimum thickness of 5.31 nm, a maximum thickness of 5.76 nm, and an average thickness of 5.49 nm, demonstrating excellent thickness uniformity of wafer-scale. Fig. 1d shows the thickness of $WS_2$ films with fixed 400 cycles under different deposition temperatures. The results show no films deposition achieved below 380 °C, and the film growth rate increases

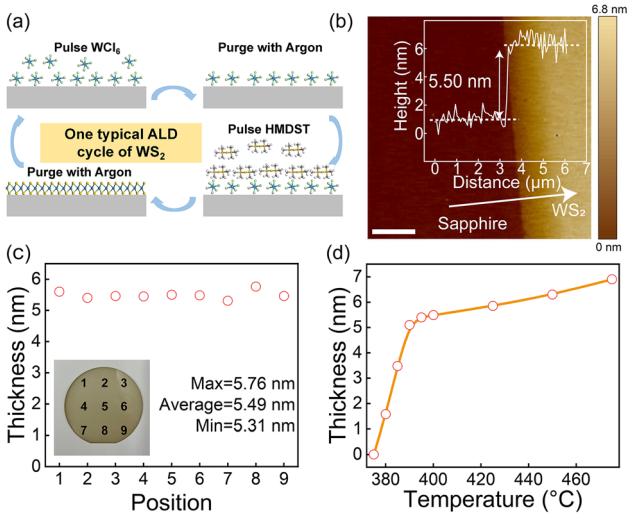


Fig. 1 (a) Process diagram of ALD $WS_2$ film. (b) The thickness of $WS_2$ film was deposited with 400 cycles at 400 °C, scalebar: 2 μm. (c) The thickness of the film in different areas on a 2-inch wafer. (d) The thickness of $WS_2$ film grown at different growth temperatures.

rapidly before 395 °C. Beyond 395 °C, the growth rate increases slowly and tends to be stable.

### 3.2 The study of deposition temperature

After obtaining the deposition window, a detailed investigation was performed to clarify the influence of deposition temperature on the quality of $WS_2$. Fig. 2a shows the AFM and XPS results of $WS_2$ films deposited at 400 °C, which presenting excellent flatness with a roughness of only 0.43 nm. Moreover, the grain of $WS_2$ can be observed, and the average grain size of $WS_2$ is about 100 nm. The XPS results show that the films consist of a mixture ratio of 4.2 for $W^{4+}$ and $W^{6+}$, and the $W^{4+}$ and $W^{6+}$ correspond to $WS_2$ and $WS_3$, indicating the product of deposition is WSX, a mixture of $WS_2$ and $WS_3$. Existence of $W^{6+}$ is mainly due to the lack of reducing environment during the ALD reaction.[34] In Fig. 2b, when the deposition temperature is 425 °C, particles appear on the surface, with the roughness increasing to 0.56 nm. The XPS results show that the ratio of $W^{4+}$ to $W^{6+}$ increases slightly to 6.4, indicating that appropriate temperature benefits the reduction of $W^{6+}$. As shown in Fig. 2c and d, with even higher deposition temperatures, the roughness of the films increases rapidly to 0.82 nm and 1.86 nm, respectively. Also in the conditions of 450 °C and 475 °C, many clumps have appeared in films. And according to the XPS analysis, the $W^{4+}/W^{6+}$ ratio decreases to 3.2 and 2.4, respectively. This indicates that above 425 °C, the precursor begins to decompose before sufficient reaction, generating large amounts of $W^{6+}$ that cannot be reduced. Thus, 400–425 °C is the preferred window for film growth, and 400 °C was selected as the optimal growth temperature due to its smoother surface.

### 3.3 The morphologies and growth mechanism of $WS_2$

In Fig. 3, AFM, high angle annular dark field-scanning transmission electron microscopy (HAADF-STEM) and SEM were applied to demonstrate the morphologies and growth process of $WS_2$. Through AFM, three types of morphologies (non-connected films, flat film, and vertical structure) can be observed corresponding to films with 200, 400, and 600 ALD cycles, respectively. Fig. 3a shows the initial nucleation stage of $WS_2$ films with 200 ALD cycles. At this stage, the size of $WS_2$

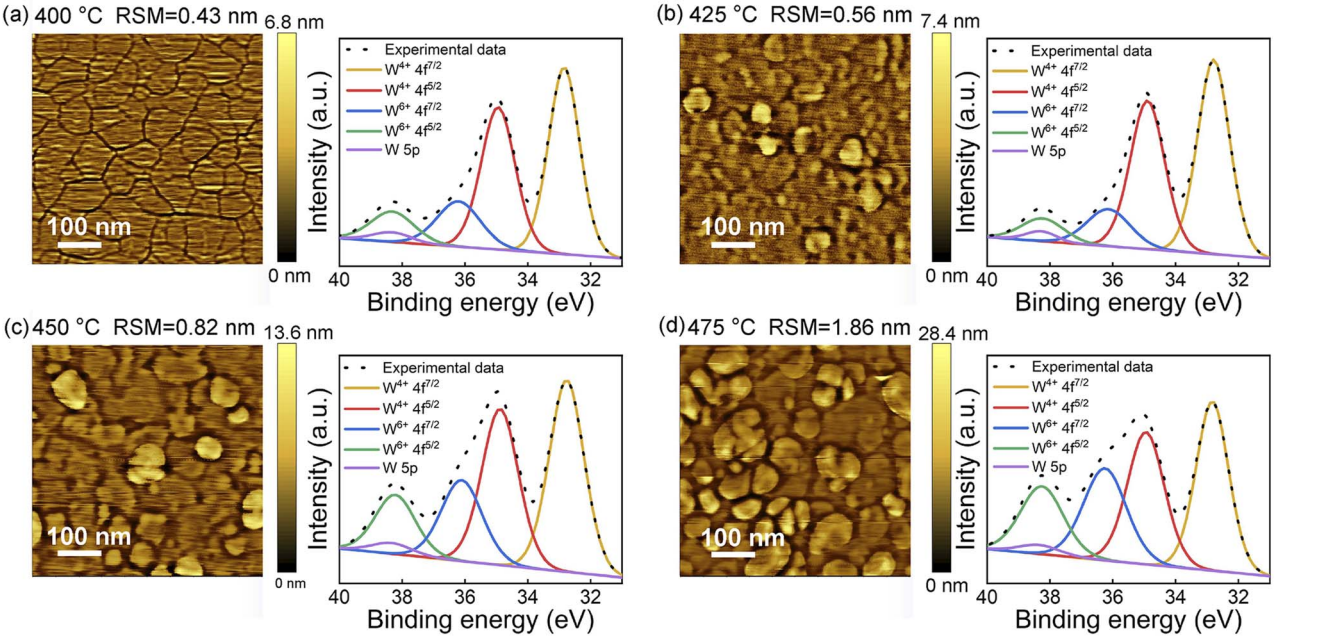


Fig. 2 Morphologies characterizations and XPS analysis of $WS_2$ films deposited at different deposition temperatures of (a) 400 °C, (b) 425 °C, (c) 450 °C, and (d) 475 °C, respectively.

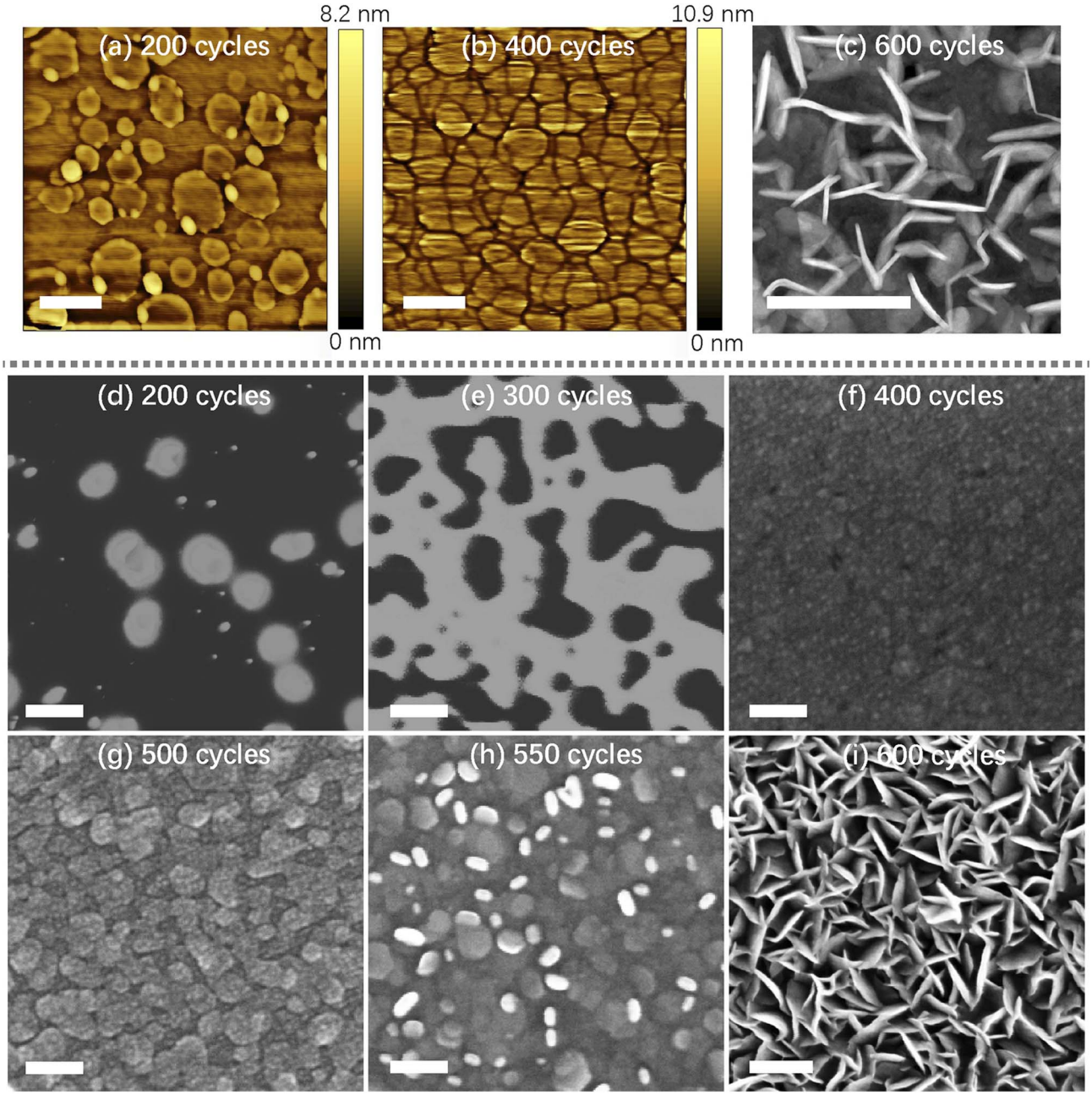


Fig. 3 The morphology of $WS_2$ films with different deposition cycles. AFM characterizations of films with (a) 200 and (b) 400 ALD cycles. (c) HAADF-STEM image of plane-view film 600 ALD cycles. (d)–(i) SEM results of samples with different ALD cycles. The scale bars in all figures are 200 nm.

varies from tens of nanometers to hundreds of nanometers, and the thickness is about 1.5 nm, corresponding to the thickness of bi-layer $WS_2$ (as shown in Fig. S3†). As shown in Fig. 3b, $WS_2$ with 400 ALD cycles result in the formation of flat films. At this stage, $WS_2$ was in horizontal growth mode, and the non-connected films were connected to form flat films. Fig. 3c shows a HAADF-STEM image of plane-view $WS_2$ film with 600 ALD cycles, a large number of $WS_2$ with nanowire structure were found. At this stage, $WS_2$ is dominated by the vertical growth mode. In Fig. 3d–i, SEM characterizations depict the growth mechanism in more detail. As shown in Fig. 3d and e, $WS_2$ gradually extend from non-connected films (with 200 ALD cycles) to interlinked network (with 300 ALD cycles). This indicates that $WS_2$ at 300 cycles was still insufficient to form a complete film. In Fig. 3f, for 400 cycles, $WS_2$ has formed a uniform film, consistent with results in AFM. $WS_2$ with 200 and 400 ALD cycles correspond to 2 and 5 layers, respectively. So in the initial growth stage, the horizontal growth rate was much higher than the vertical growth, and no warping microstructures was observed. This is because the edge of $WS_2$ performs better precursor adsorption than the base surface, so $WS_2$ is more likely to nucleate along the edge of the film rather than on

the film's surface.[35] Fig. 3g corresponds to $WS_2$ film with 500 ALD cycles, with visible grains. In this period, an upward warping trend appears at the junction of $WS_2$. This phenomenon can be attributed to the fact that after the island structure connect, the precursor is more likely to adsorb at the grain boundary between adjacent grains. In addition, the strain at grain boundaries will continuously accumulate, which changes the growth direction of $WS_2$.[28] As shown in Fig. 3h, for 550 cycles, these warped parts overgrow, and the junction of island nanosheets is covered with vertical $WS_2$. At this stage, the reactive active site of the reaction is warped at the edge, so $WS_2$ grows rapidly along the vertical direction. Fig. 3i shows $WS_2$ films with 600 ALD cycles, where the surface of $WS_2$ has already been covered with dense vertical $WS_2$. It is worth noting that the morphology of $WS_2$ will not change significantly if the ALD cycles continue to increase (as shown in Fig. S4†).

### 3.4 Annealing and doping process of $WS_2$

Fig. 4 shows a post-annealing process to improve the quality of films in the S atmosphere. Fig. 4a shows the Raman spectra at different annealing temperatures. $E^1_{2g}$ and $A_{1g}$ represent the in-plane and out-of-plane vibration modes of $WS_2$, respectively.[36] With the increase of annealing temperature, the intensity of peak $E^1_{2g}$ increases significantly, which confirms the film crystallinity can be improved availably by annealing. In Fig. 4b, after 950 °C for 2 hours annealing, the fine spectra of W 4f exhibited only one pair of W $4f^{5/2}$ and W $4f^{7/2}$ peaks, indicating the $W^{6+}$ have been reduced to $W^{4+}$, along with a similar result for S 2p spectra, both without characteristic peaks indicative of $W^{6+}$–S bonding. After annealing, the stoichiometric ratio of W/S was reduced to 1 : 2. Fig. 4c shows deposited and annealed TEM of $WS_2$; the average thickness of $WS_2$ film is about 4.7 nm, and the number of layers is 5. Compared to unannealed film, the annealed $WS_2$ film has a more smooth and clear layered structure. It can be demonstrated that post-annealing is critical for $WS_2$ film grown by ALD, which can significantly improve the crystallinity, optimize the proportion of elements and smooth the lamellar structure of the film.

ALD can accurately dope $WS_2$ films by introducing doping precursors.[37] Nb-doped $WS_2$ has been proved that the acceptor energy level appears at the top of the valence band of $WS_2$, which can achieve P-type semiconductor characteristics.[38] In addition, compared with other elements, Nb substituted W has lower formation energy and slight local distortion, and Nb can remain stable through covalent bonds within the lattice.[39] $WS_2$ is natively an N-type, which origin is existence of native sulfur vacancies provided omnipresent electron donating. When Nb with five valence electrons replaces W with six valence electrons, one electron is removed from the system to keep the total charge neutrality, causing the top valence band becomes

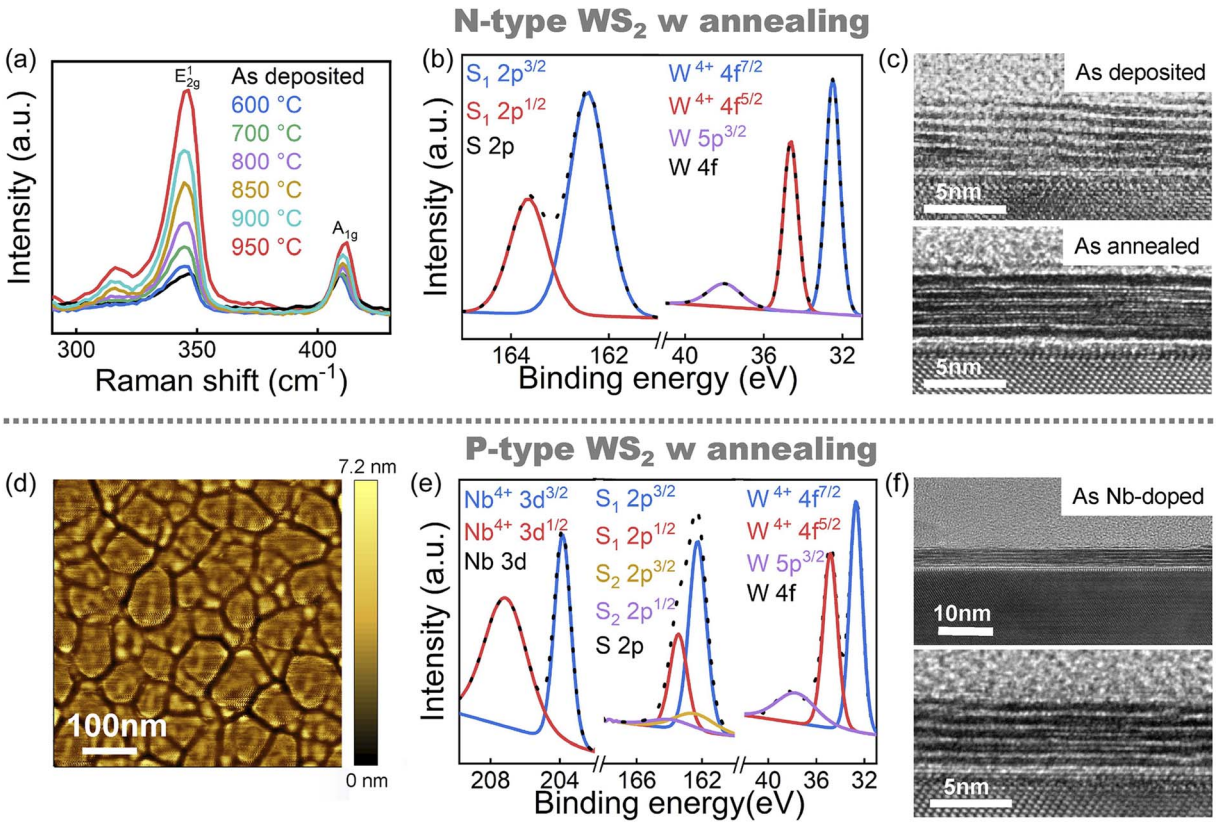


Fig. 4 (a) Raman spectra of $WS_2$ at different annealed temperatures. (b) XPS spectra of $WS_2$ at 950 °C annealed temperature. ($S_1$ stands for $S^{2-}$–$W^{4+}$ bonding) (c) the cross-sectional TEM results for deposited and annealed $WS_2$ film. (d) AFM, (e) XPS ($S_2$ stands for $S^{2-}$–$Nb^{4+}$ bonding), and (f) TEM of Nb-doped $WS_2$ film.

electron deficient, and the system becomes hole-rich and P-doped.[40] Therefore, Nb is a suitable doping element for preparing P-type $WS_2$ films. Nb doping can be easily controlled by programming ALD deposition process. Next, $NbCl_5$ is added to the $WS_2$ process as a doping precursor for preparing P-type $WS_2$ film (detailed doping process in Fig. S5†). The annealing process of P- type $WS_2$ is the same as that of N-type $WS_2$. Fig. 4d shows the AFM image of Nb-doped $WS_2$, with a roughness of 0.48 nm, which is not distinguishable from the undoped $WS_2$ film. This indicates that Nb doping will not break the surface smoothness of $WS_2$ films. In Fig. 4e, XPS proves the existence of Nb in P-type $WS_2$. A fine spectrum can prove that Nb is doped into $WS_2$ as $Nb^{4+}$. W 4f fine spectrum in P-type $WS_2$ also only demonstrate a pair of characteristic peaks $W^{4+}$ $4f^{7/2}$ and $W^{4+}$ $4f^{5/2}$, which is consistent with N-type $WS_2$. The difference is in the fine spectrum of S, in addition to the characteristic peaks of W–S, the characteristic peaks of Nb–S are also observed, indicating that both $Nb^{4+}$ and $W^{4+}$ are bonded to $S^{2-}$. Fig. 4f shows the TEM of Nb-doped $WS_2$ film, compared with undoped $WS_2$ thin films, Nb doping does not significantly damage the original flat layered structure. The results indicate that Nb is a non-destructive effective doping for ALD-grown $WS_2$.

### 3.5 Functionalized device applications

The in-plane conductivity of $WS_2$ is 8–70 times that of the out-of-plane direction.[41] So flat $WS_2$ film can be used as a functional material for FETs, and vertical $WS_2$ is more suitable for preparing gas sensors because the vertical structure can provide more abundant morphology and expose more adsorption sites.[42] As shown in Fig. 5a, we selected flat film to prepare the FET array. Fig. 5b shows the transfer characteristic of the N- and P-type FET based on $WS_2$ film at $V_{DS} = 0.5$ V. The devices show typical N and P type transfer characteristic before and after Nb-doped, respectively. The red dash line shows the N-FETs transfer curve under 800 °C annealed. Compared with 950 °C annealed devices, although the devices exhibit N- type FET characteristics, the $I_{on}$ is reduced by two orders of magnitude, with a $I_{on}/I_{off}$ ratio of only $10^2$. The poor performance can be attributed to the low crystallinity of $WS_2$ annealed at 800 °C, and there is still defects in $WS_2$ film. For 950 °C annealed N-FET, the $\mu_{FE}$ is 7.25 $cm^2\ V^{-1}\ s^{-1}$, and the $I_{on}/I_{off}$ is above $10^5$. And for P-FET, the $\mu_{FE}$ is 0.23 $cm^2\ V^{-1}\ s^{-1}$, and the $I_{on}/I_{off}$ is above $10^2$. In Fig. 5c and d, without Nb-doped $WS_2$ FETs show typical N-type output characteristic, and Nb-doped $WS_2$ FETs show typical P-type output characteristic. The current tends to saturate at $V_{DS} = 5$ V. This indicates that the carrier type of $WS_2$ FETs can indeed be changed from electron to hole by Nb doping.

Fig. 5e shows a schematic of a gas sensor. In Fig. 5f, the response of horizontal and vertical N-type $WS_2$ and Nb-doped P-type $WS_2$ to $NH_3$ at room temperature was measured, respectively. The gas response was calculated according to the following relation: $\Delta R/R_a = (R_g - R_a)/R_a$, where $R_a$ and $R_g$ are the resistances of the sensing devices to the air and analyte gases, respectively. The response of flat and vertical N-type $WS_2$ is 6% and 14%, respectively. Nb-doped nanomaterials have been proven to be a promising method for improving gas sensing performance.[43] In Fig. 5g, to further demonstrate highly enhanced gas response properties in Nb-doped $WS_2$ film, resistance variations of P-type films to diluted $NH_3$ (5–100 ppm) gas are measured. The P-type vertical $WS_2$ gas sensor shows a significantly high response (42%) to 50 ppm $NH_3$ exposure at room temperature. Fig. 5h shows the comparative response to

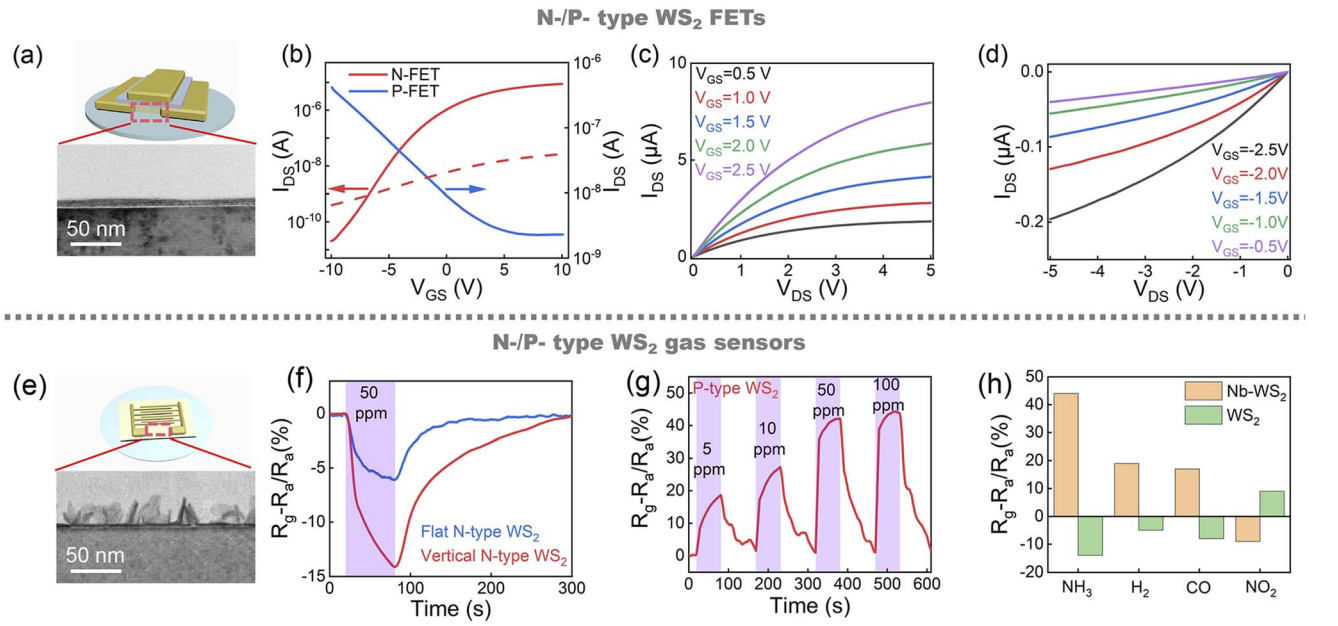


Fig. 5 (a) Schematic illustration of top-gated $WS_2$ FET on a sapphire substrate. (b) Transfer characteristics of N-type and P-type $WS_2$ FETs at $V_{DS} = 0.5$ V. Output characteristics of (c) N-type and (d) P-type $WS_2$ FETs. (e) Schematic illustration of $WS_2$ gas sensor. (f) Response to $NH_3$ exposure of flat and vertical $WS_2$ gas sensors. (g) Response to $NH_3$ exposure of vertical P-type $WS_2$ gas sensors. (h) Selectivity of vertical N- and P-type $WS_2$ gas sensors upon exposure to various gases (50 ppm $NH_3$, $H_2$, CO, and $NO_2$, respectively).

various gases. For P-type $WS_2$, a positive response was shown upon $NH_3$, $H_2$, or CO exposure, while a negative response occurred with exposure to $NO_2$. The response of N-type $WS_2$ is opposite to that of P-type $WS_2$. This is related to the different adsorption energy and degree of charge transfer to various gases.[44] It is also very evident that the $NH_3$ response is much higher than other gases.

## 4. Conclusions

In this work, we demonstrate ALD-$WS_2$ processes during which morphologies and doping type can be flexibly regulated based on different requirements for various device applications. First, by studying the deposition temperature, growth mechanism, and annealing conditions of $WS_2$ deposited by ALD, high-quality wafer-scale N-type $WS_2$ films were prepared. Then, ALD can excellently regulate the morphologies and Nb-doping to obtain ideal P-type $WS_2$ films. Finally, we successfully prepared high-performance N-type and P-type FETs with flat $WS_2$ film and prepared N-type and P-type gas sensors with vertical $WS_2$. Nb doping can regulate carrier types and significantly improve the response of gas sensors. The results show that morphologies and doping type of $WS_2$ films can be regulated simply by adjusting and programming the ALD processes, and can be well applied to FETs and gas sensors.

## Author contributions

The manuscript was written through contributions of all authors. All the authors have given approval to the final version of the manuscript.

## Conflicts of interest

There are no conflicts to declare.

## Acknowledgements

This work is partially supported by NSFC (62004044 and 62204048). L. J. acknowledges the support of the starting research fund from Fudan University and the support by State Key Laboratory of ASIC & System (2021MS004).

## Notes and references

1 J. Shim, H. Y. Park, D. H. Kang, J. O. Kim, S. H. Jo, Y. Park and J. H. Park, *Adv. Electron. Mater.*, 2017, **3**, 1600364.
2 X. Wang, J. Song and J. Qu, *Angew. Chem., Int. Ed.*, 2019, **58**, 1574.
3 C. Xie, C. Mak, X. Tao and F. Yan, *Adv. Funct. Mater.*, 2017, **27**, 1603886.
4 S. Y. Kim, J. Kwak, C. V. Ciobanu and S. Y. Kwon, *Adv. Mater.*, 2019, **31**, 1804939.
5 G. H. Park, K. Nielsch and A. Thomas, *Adv. Mater. Interfaces*, 2019, **6**, 1800688.
6 K. F. Mak and j. Shan, *Nat. Photonics*, 2016, **10**, 216.
7 W. Choi, N. Choudhary, G. H. Han, J. Park, D. Akinwande and Y. H. Lee, *Mater. Today*, 2017, **20**, 3.
8 A. B. Kaul, *J. Mater. Res.*, 2014, **29**, 348.
9 C. Lan, C. Li, J. C. Ho and Y. Liu, *Adv. Electron. Mater.*, 2021, **7**, 2000688.
10 W. Zhang, Z. Huang, W. Zhang and Y. Li, *Nano Res.*, 2014, **7**, 1731.
11 Z. Ye, T. Cao, K. O'brien, H. Zhu, X. Yin, Y. Wang, S. G. Louie and X. Zhang, *Nature*, 2014, **513**, 214.
12 Z. Y. Zhu, Y. C. Cheng and U. Schwingenschlögl, *Phys. Rev. B: Condens. Matter Mater. Phys.*, 2011, **84**, 153402.
13 W. Zhao, Z. Ghorannevis, L. Chu, M. Toh, C. Kloc, P. H. Tan and G. Eda, *ACS Nano*, 2013, **7**, 791.
14 Y. G. You, D. H. Shin, J. H. Ryu, E. E. B. Campbell, H. J. Chung and S. H. Jhang, *Nanotechnology*, 2021, **32**, 505702.
15 A. Rawat, N. Jena and A. D. Sarkar, *J. Mater. Chem. A*, 2018, **6**, 8693.
16 M. W. Iqbal, K. Shahzad, G. Hussain, M. K. Arshad, R. Akbar, S. Azam, S. Aftab, T. Alharbi and A. Majid, *Mater. Res. Express*, 2019, **6**, 115909.
17 S. Tongay, W. Fan, J. Kang, J. Park, U. Koldemir, J. Suh, D. S. Narang, K. Liu, J. Ji and J. Li, *Nano Lett.*, 2014, **14**, 3185.
18 P. Bhattacharyya and D. Acharyya, *IEEE Sens. J.*, 2021, **21**, 22414.
19 A. Sebastian, R. Pendurthi, T. H. Choudhury, J. M. Redwing and S. Das, *Nat. Commun.*, 2021, **12**, 693.
20 Y. Wan, E. Li, Z. Yu, J. K. Huang, M. Y. Li, A. S. Chou, Y. T. Lee, C. J. Lee, H. C. Hsu, Q. Zhan, A. Aljarb, J. H. Fu, S. P. Chiu, X. Wang, J. J. Lin, Y. P. Chiu, W. H. Chang, H. Wang, Y. Shi, N. Lin, Y. Cheng, V. Tung and L. J. Li, *Nat. Commun.*, 2022, **13**, 4119.
21 W. T. Koo, J. H. Cha, J. W. Jung, S. J. Choi, J. S. Jang, D. H. Kim and I. D. Kim, *Adv. Funct. Mater.*, 2018, **28**, 1802575.
22 H. Tang, Y. Li, R. Sokolovskij, L. Sacco, H. Zheng, H. Ye, H. Yu, X. Fan, H. Tian, T. L. Ren and G. Zhang, *ACS Appl. Mater. Interfaces*, 2019, **11**, 40850–40859.
23 W. Gao, S. Zhang, F. Zhang, P. Wen, L. Zhang, Y. Sun, H. Chen, Z. Zheng, M. Yang, D. Luo, N. Huo and J. Li, *Adv. Electron. Mater.*, 2021, **7**, 2000964.
24 J. Gu, B. Chakraborty, M. Khatoniar and V. M. Menon, *Nat. Nanotechnol.*, 2019, **14**, 1024.
25 T. Nam, S. Seo and H. Kim, *J. Vac. Sci. Technol.*, 2020, **38**, 030803.
26 S. W. Nam, M. J. Rooks, K. B. Kim and S. M. Rossnagel, *Nano Lett.*, 2009, **9**, 2044.
27 N. Wei, N. Gao, H. Xu, Z. Liu, L. Gao, H. Jiang, Y. Tian, Y. Chen, X. Du and L. M. Peng, *Nano Res.*, 2022, **15**, 9876.
28 H. Yang, Y. Wang, X. Zou, R. X. Bai, S. Han, Z. Wu, Q. Han, Y. Zhang, H. Zhu, L. Chen, X. Lu, Q. Sun, J. C. Lee, E. T. Yu, D. Akinwande and L. Ji, *ACS Appl. Mater. Interfaces*, 2021, **13**, 43115.
29 H. Yang, Y. Wang, X. Zou, R. Bai, Z. Wu, S. Han, T. Chen, S. Hu, L. Chen, D. W. Zhang, J. C. Lee, X. Lu, P. Zhou, Q. Sun, E. T. Yu, D. Akinwande and L. Ji, *Research*, 2021, 9862483.

30 B. Groven, A. N. Mehta, H. Bender, J. Meersschaut, T. Nuytten, P. Verdonck, T. Conard, Q. Smets, T. Schram, B. Schoenaers, A. Stesmans, V. Afanaśev, W. Vandervorst, M. Heyns, M. Caymax, I. Radu and A. Delabie, *Chem. Mater.*, 2018, **30**, 7648.
31 Y. Jang, S. Yeo, H. B. R. Lee, H. Kim and S. H. Kim, *Appl. Surf. Sci.*, 2016, **365**, 160.
32 Y. Huang, L. Liu, J. Sha and Y. Chen, *Appl. Phys. Lett.*, 2017, **111**, 063902.
33 M. Chhowalla, H. S. Shin, G. Eda, L. J. Li, K. P. Loh and H. Zhang, *Nat. Chem.*, 2013, **5**, 263.
34 Y. Wu, M. H. Raza, Y. C. Chen, P. Amsalem, S. Wahl, K. Skrodczky, X. Xu, K. S. Lokare, M. Zhukush, P. Gaval, N. Koch, E. A. Quadrell and N. Pinna, *Chem. Mater.*, 2019, **31**, 1881.
35 S. Balasubramanyam, M. Shirazi, M. A. Bloodgood, L. Wu, M. A. Verheijen, V. Vandalon, W. M. M. Kessels, J. P. Hofmann and A. A. Bol, *Chem. Mater.*, 2019, **31**, 5104.
36 X. Huang, Y. Gao, T. Yang, W. Ren, H. M. Cheng and T. Lai, *Sci. Rep.*, 2016, **6**, 1.
37 V. Vandalon, M. Verheijen, W. Kessels and A. Bol, *ACS Appl. Nano Mater.*, 2020, **3**, 10200.
38 Y. Jin, Z. Zeng, Z. Xu, Y. C. Lin, K. Bi, G. Shao, T. S. Hu, S. Wang, S. Li, K. Suenaga, H. Duan and Y. Feng, *Chem. Mater.*, 2019, **31**, 3534.
39 N. Li, Z. Liu, S. Hu and H. Wang, *Solid State Commun.*, 2018, **269**, 58.
40 J. Gao, Y. D. Kim, L. B. Liang, J. C. Idrobo, P. Chow, J. Tan, B. Li, L. Li, B. G. Sumpter, T. M. Lu, V. Meunier, J. Hone and N. Koratkar, *Adv. Mater.*, 2016, **28**, 9735.
41 A. Pisoni, J. Jacimovic, R. Gaál, B. Náfrádi, H. Berger, Z. Révay and L. Forró, *Scr. Mater.*, 2016, **114**, 48.
42 S. Y. Cho, S. J. Kim, Y. Lee, J. S. Kim, W. B. Jung, H. W. Yoo, J. Kim and H. T. Jung, *ACS Nano*, 2015, **9**, 9314.
43 S. Y. Cho, Y. Kim, H. S. Chung, A. R. Kim, J. D. Kwon, J. Park, Y. L. Kim, S. H. Kwon, M. G. Hahm and B. Cho, *ACS Appl. Mater. Interfaces*, 2017, **9**, 3817.
44 B. Cho, M. G. Hahm, M. Choi, J. Yoon, A. R. Kim, Y.-J. Lee, S.-G. Park, J.-D. Kwon, C. S. Kim, M. Song, Y. Jeong, K.-S. Nam, S. Lee, T. J. Yoo, C. G. Kang, B. H. Lee, H. C. Ko, P. M. Ajayan and D.-H. Kim, *Sci. Rep.*, 2015, **5**, 8052.